S Supplement

S.1 Supplemental Figures

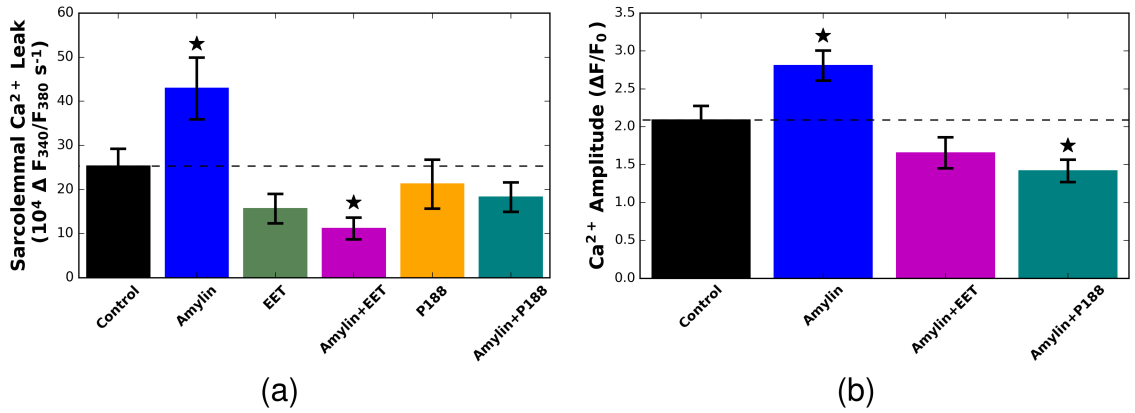

Figure S1: Effect of human amylin on sarcolemmal Ca^{2+} leak and intracellular Ca^{2+} transient amplitude. a) Outward sarcolemmal Ca^{2+} leaks are reported for control (n=13) and amylin-incubated rat cardiomyocytes (n=12). Significantly higher sarcolemmal leak rates were found for cardiomyocytes incubated with amylin relative to control. Co-incubation with the membrane sealant P188 (n=5) and the pro-fibrinolytic agent EET (n=5) prevented the amylin-induced increase in sarcolemmal Ca^{2+} leak. b) Amplitudes of Ca^{2+} transients in control myocytes (n=12) and myocytes incubated with human amylin in the absence (n=10) and in the presence of P188 (n=8) or EET (n=5). $^{*}P < 0.05$

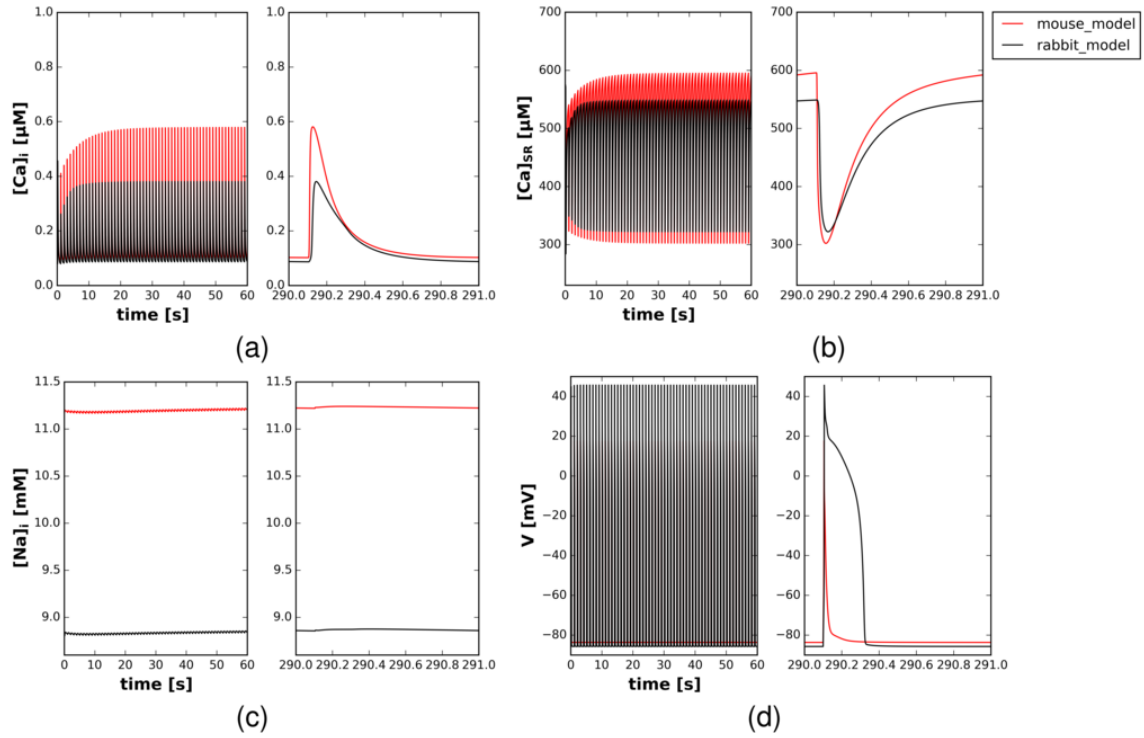

Figure S2: Predicted intracellular Ca^{2+} (a), sarcoplasmic reticulum Ca^{2+} (b), intracellular sodium (c), and action potential (d) for mouse (red) and rabbit (black) conditions

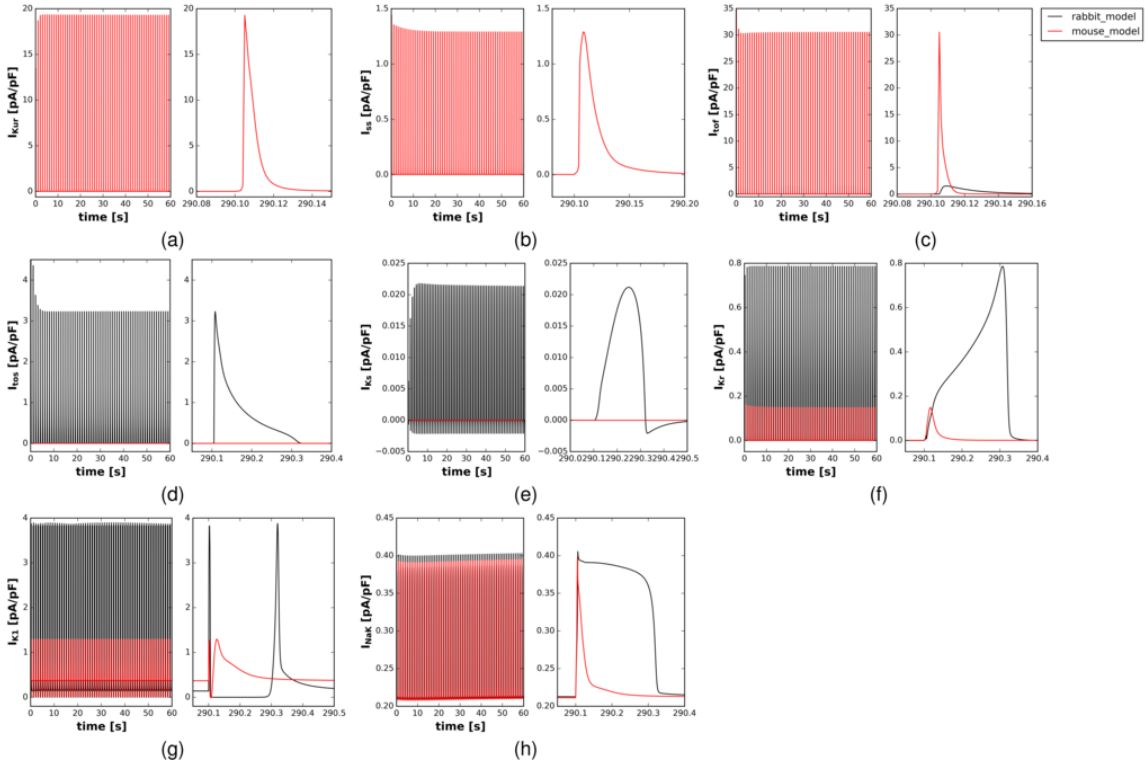

Figure S3: Comparison of potassium currents predicted for rabbit (black) and mouse (red) ventricular cardiomyocytes via the SB and SBM models, respectively. Top row, from left: slowly inactivating current, i_{kur}, steady-state current, i_{ss}, fast transient outward current, i_{tof}. Middle row: slow transient outward current, i_{tos}, slowly activating current, i_{Ks}, rapidly activating current, i_{Kr}. Bottom row: inward rectifier current, i_{K1}, sodium/potassium exchanger, i_{NaK}

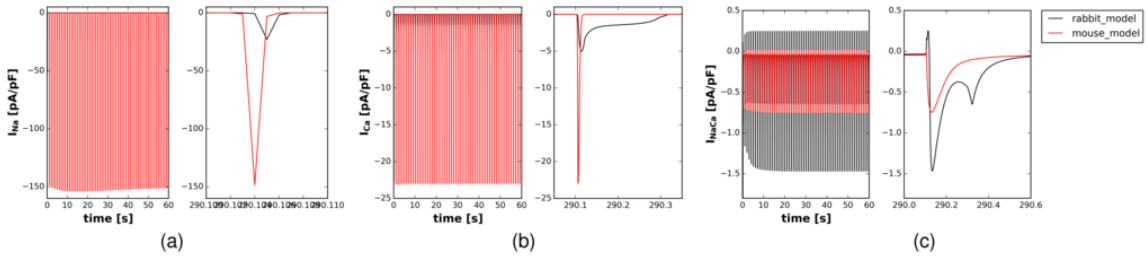

Figure S4: Comparison of sodium current (Left), i_{Na}, L-type Ca^{2+} channel current (middle), i_{CaL}, and sodium/Ca^{2+}-exchanger current (right), i_{NaCa}, predicted for rabbit (black) and mouse (red) ventricular cardiomyocytes via the SB and SBM models, respectively.

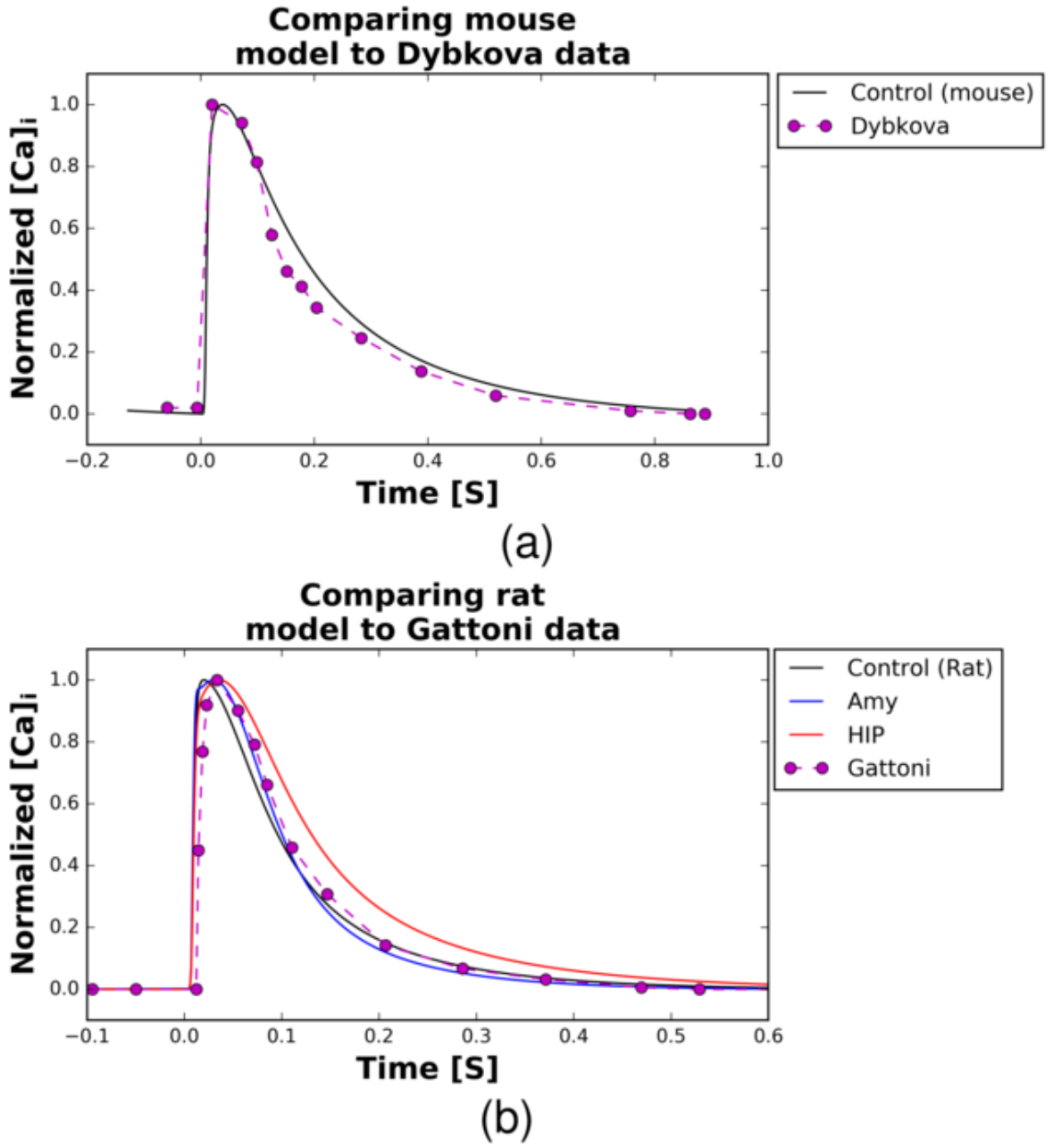

Figure S5: Comparison of experimental Ca^{2+} transient data (Dybkova) at 1 Hz for mouse (a)[29, 70] and rat (Gattoni) (b)[25] (purple) with our predicted control data (black). Ca^{2+} transients predicted for +Amylin (blue) and HIP (red) are additionally provided.

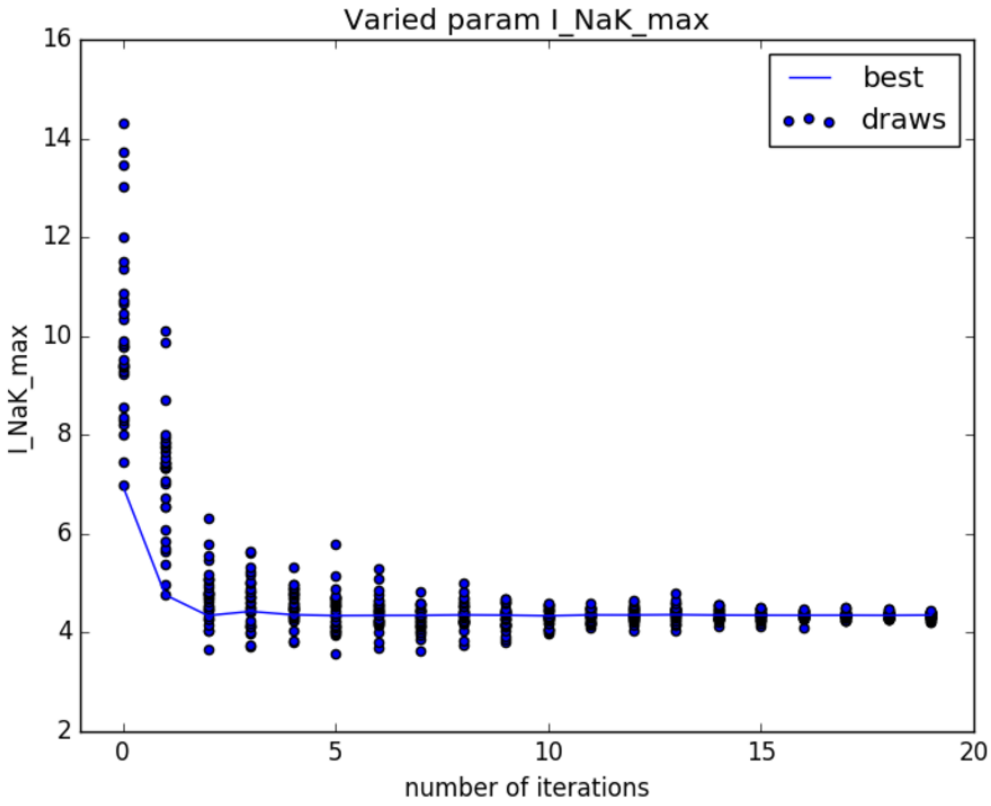

Figure S6: Verification of the genetic algorithm used to fit the mouse model to the rat model. Many random draws were made for each iteration with the best random draw chosen. The best random draw becomes the new starting point random draws are made around for the next iteration. Each iteration was given a smaller range to randomize over in order to converge the system. As can be seen, the system converged to single value after completing several iterations

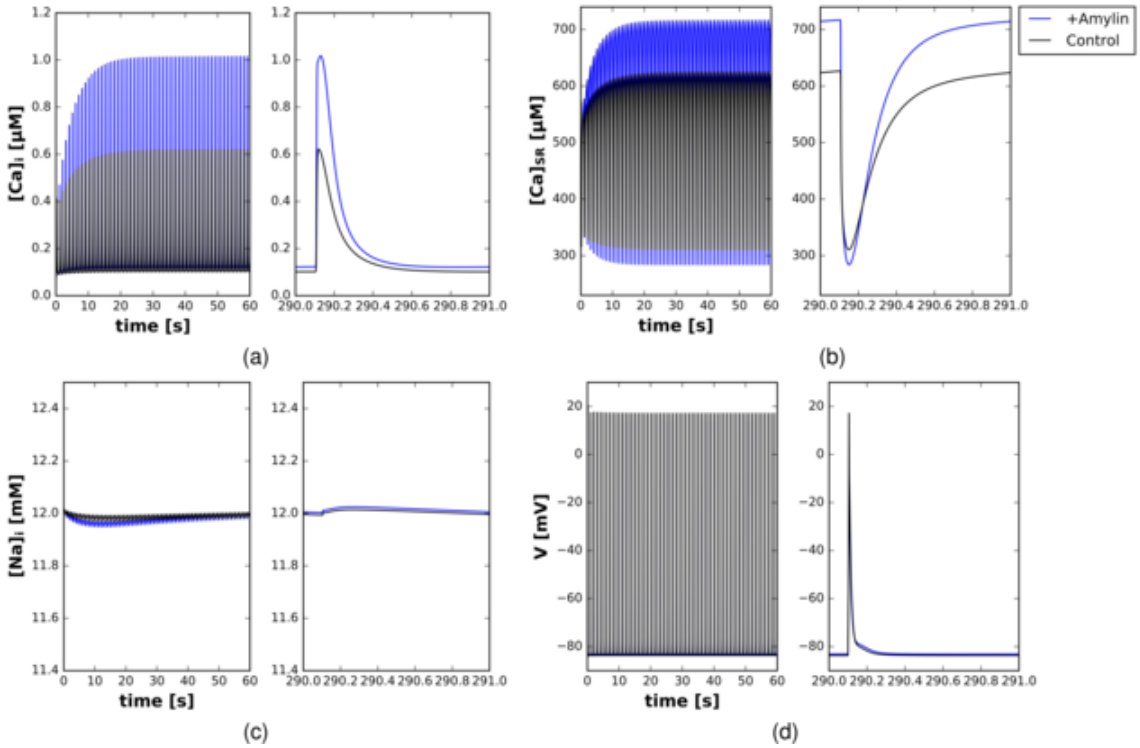

Figure S7: Predicted intracellular Ca^{2+} (a), sarcoplasmic reticulum Ca^{2+} (b), intracellular sodium (c), and action potential (d) for control (black) and +Amylin (blue) conditions. Results are presented for 0 to 60s for clarity, although action potentials for up to 300s are reported in Fig. S13.

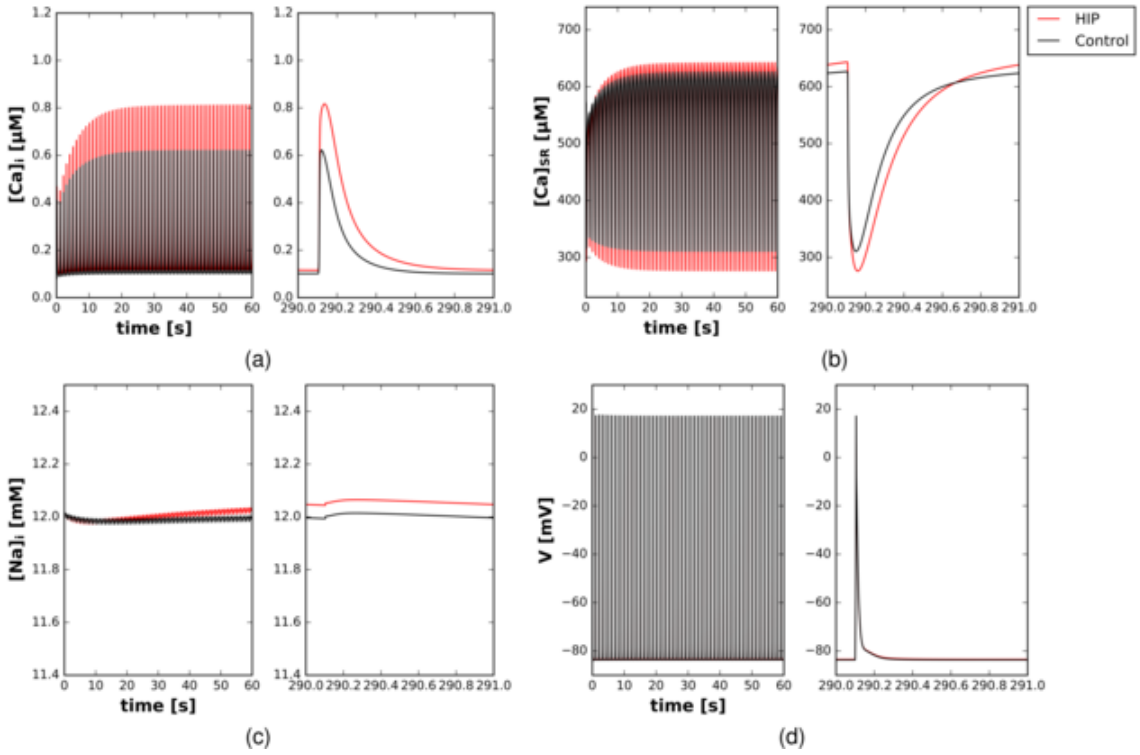

Figure S8: Predicted intracellular Ca^{2+} (a), sarcoplasmic reticulum Ca^{2+} (b), intracellular sodium (c), and action potential (d) for control (black) and HIP (red) conditions. Results are presented for 0 to 60s for clarity, we report full 300s simulations in Fig. S13

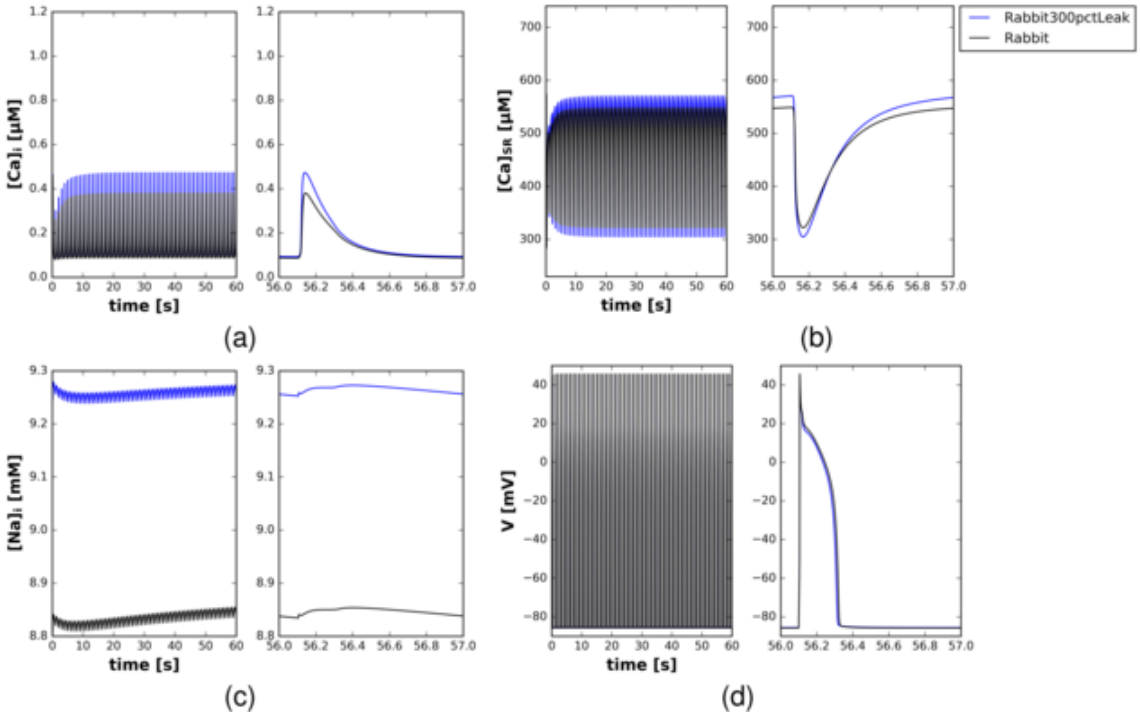

Figure S9: Predicted intracellular Ca^{2+} (a), sarcoplasmic reticulum Ca^{2+} (b), intracellular sodium (c), and action potential (d) for control (black) and 300 % increased Ca^{2+} background leak (blue) conditions using the rabbit SB model.

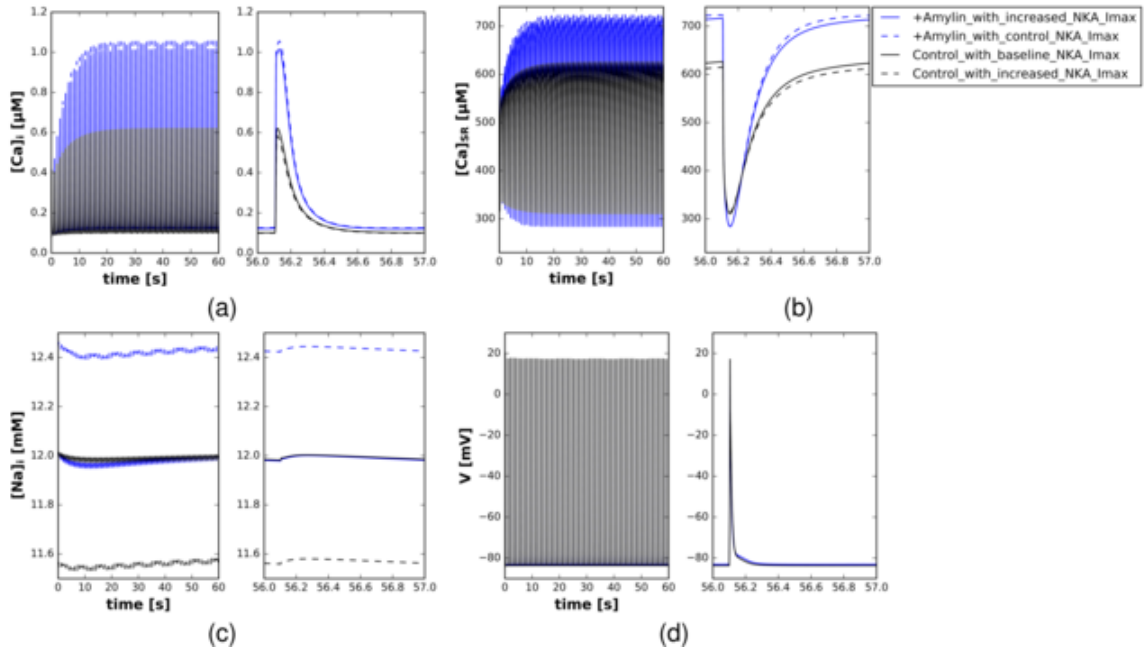

Figure S10: Simulated contributions of SL sodium/potassium ATPase activity to intracellular Ca^{2+} and Na^{+} load. Predicted a) Ca^{2+} and b) Na^{+} intracellular transients under control (black, solid line), control with increased NKA to match +Amylin level NKA current(black, dashed line), +Amylin (blue, solid line), and +Amylin with decreased NKA to match control level NKA current (blue, dashed line). See Table S3 for parameters.

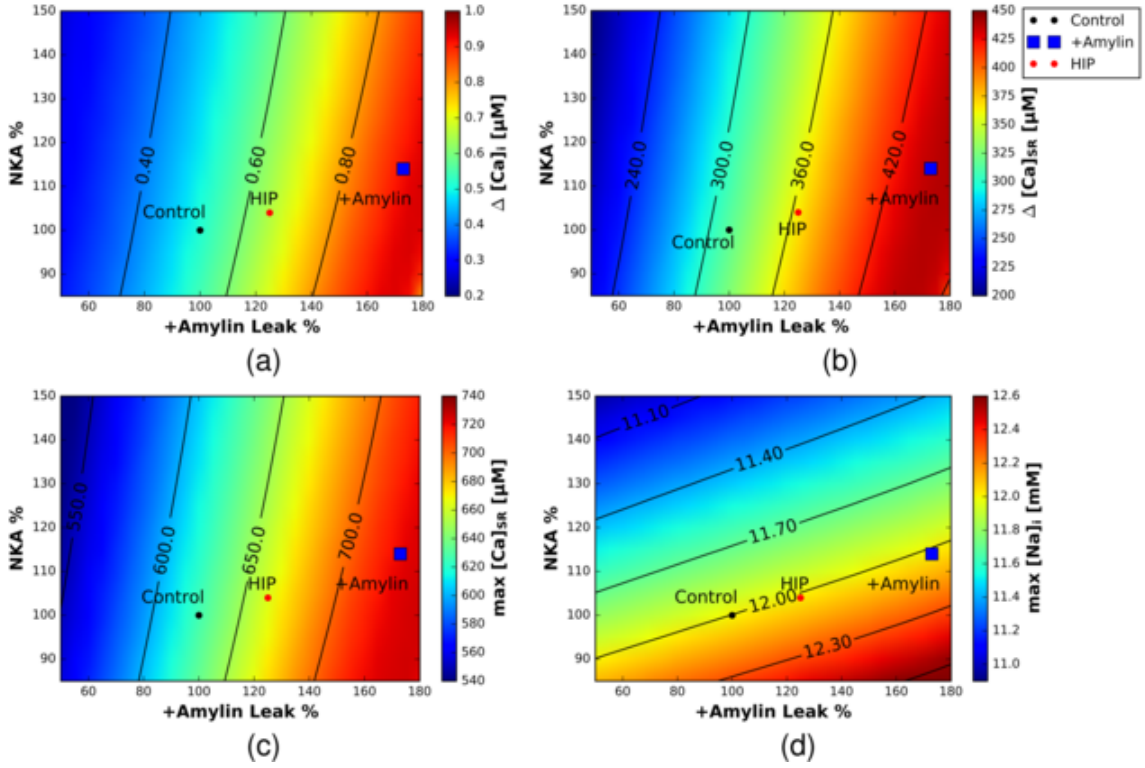

Figure S11: Predicted Ca^{2+} transients and loads as a function of NKA activity (% of control) and SL Ca^{2+} leak (% of control). a) intracellular Ca^{2+}, b) SR Ca^{2+} transient c) maximum SR Ca^{2+} load and d) sodium load. A black point is representative of the Control case, a blue square is representative of the Amy case, and a red point is representative of the HIP case. Measurements are taken at 55 s

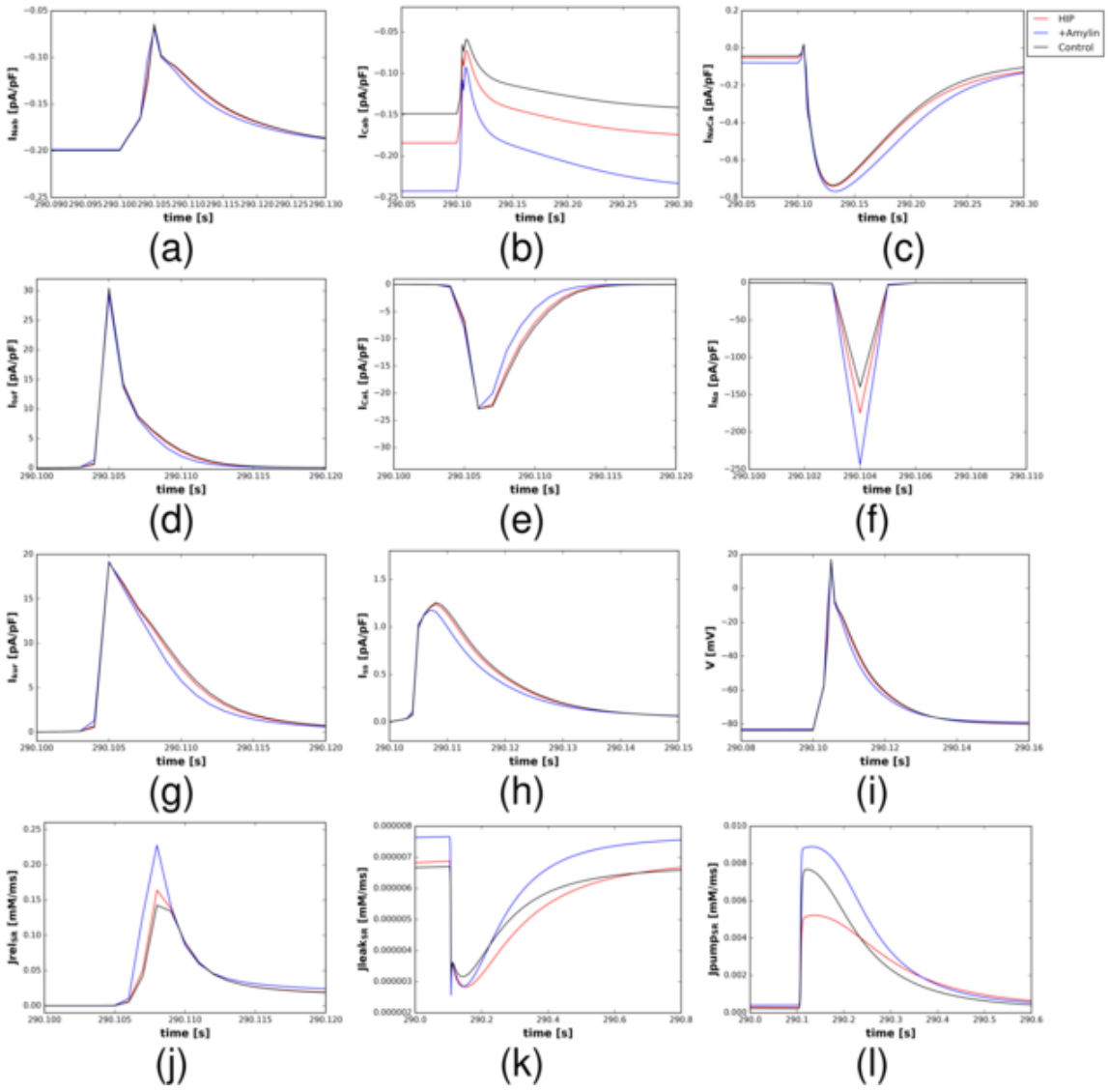

Figure S12: Fluxes and currents for control (black), +Amylin(blue), and HIP(red) conditions

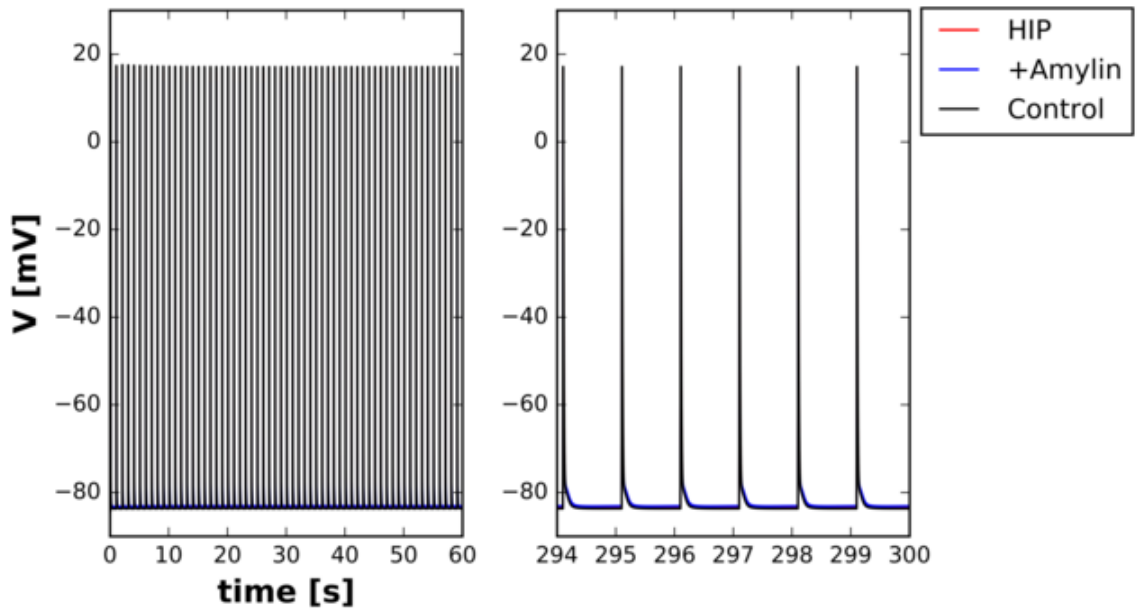

Figure S13: Predicted action potential, V, for control, +Amylin, and HIP-conditions over five minutes of 1 Hz pacing to demonstrate model stability

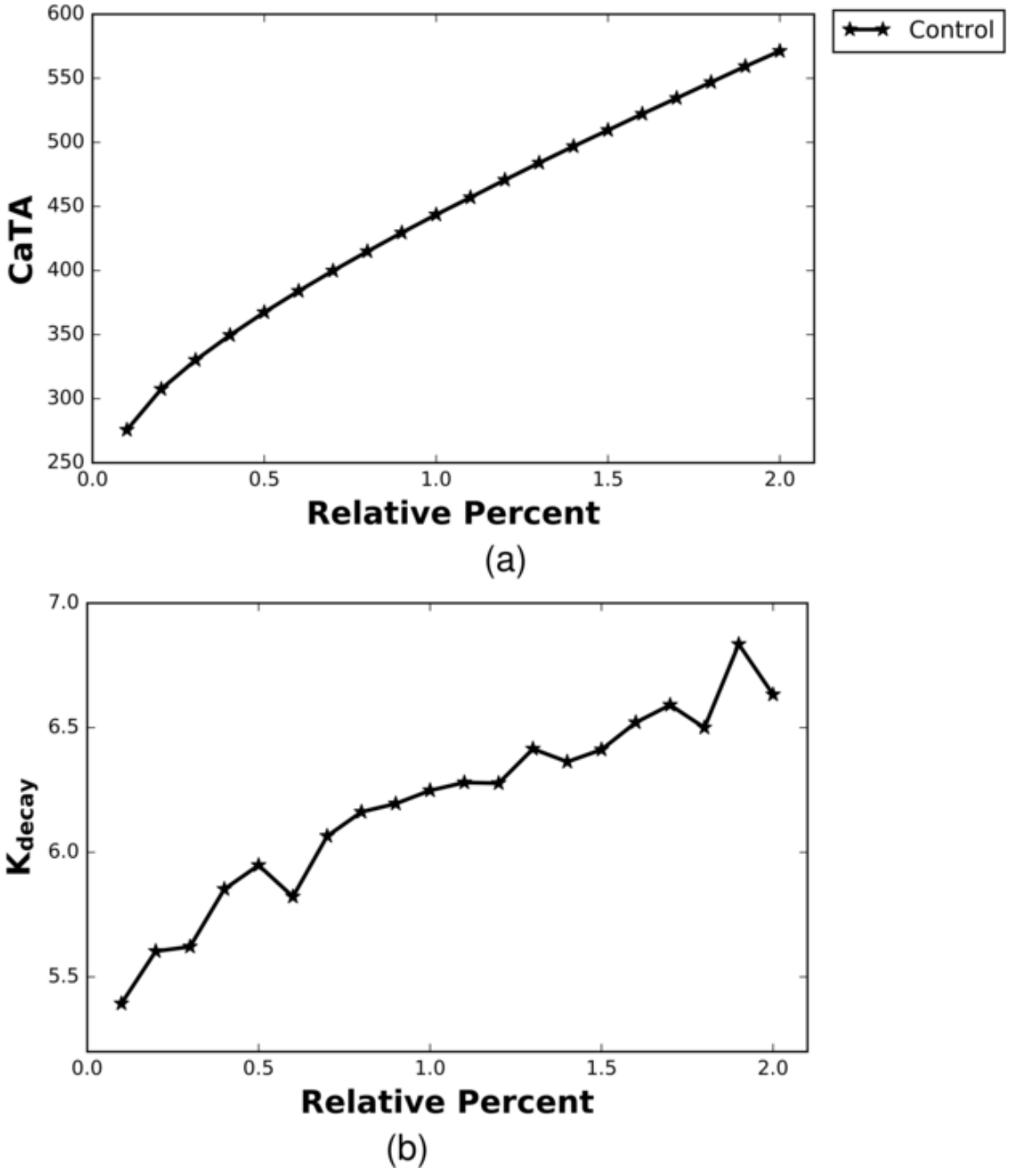

Figure S14: a) Ca^{2+} transient amplitudes (CaTA) and b) Ca^{2+} transient decay rates (Kdecay) as a function of SL Ca^{2+} leak, using the rat ventricular cardiomyocyte model from Dvenyi et al [26]. 1.0 corresponds to the SL Ca^{2+} leak rate default value (normalized). Trends predicted by the Dvenyi et al are analogous to those we report with our SBM implementation.

S.2 Supplemental Tables

Table S1: Comparison of SB default parameters with mouse-specific variations in accordance to Morotti et al. [29] Places with * represent the value was fitted using our GA to match corresponding experimental data.

Parameter [units]	Name	Rabbit	Mouse	Rat
Membrane capacitance [F]	C_m	1.381×10^{-10}	2.0×10^{-10}	-
Cell volume [L]	V_{Cell}	3.04×10^{-11}	3.30×10^{-11}[29]	-
Intracellular Na^+[mM]	Na_i	8.80853	11.1823	12.0
Free concentration of Ca^{2+} in extracellular compartment [mM]	$[Ca]_o$	1.8	1.0	-
Maximal conductance of flux for fast Na^+ current [mS µF^{-1}]	G_{INa}	16	10	-
Junctional partitioning	F_{Xi} junction	0.11	0.19	-
Sarcolemmal partitioning	F_{Xi} sarcolemmal	0.89	0.81	-
Background Na^+ leak [mS µF^{-1}]	G_{NaBk}	2.97×10^{-4}	1.337×10^{-3}	-
K˙m of Na^+ - Ca^{2+} exchanger for Na^+ [mM]	K_{mNai}	11	19	-
Max current of the Na^+ - K^+ pump [µA µF^{-1}]	I_{NaKmax}	1.90719	5.0	*
Slow activating delayed rectifier current	G_{Ks}	1.0	0.0	-
Slow inactivating delayed rectifier current 1 [nS pF^{-1}]	$Gkur1$	N/A	0.176	-
Slow inactivating delayed rectifier current 2 [nS pF^{-1}]	$Gkur2$	N/A	0.14	-
i_{SS}conductance [nS pF^{-1}]	Gss	N/A	0.15	-
Velocity max for Na^+ - Ca^{2+} exchanger [µA µF^{-1}]	$V_{maxINaCa}$	9	1	-
Allosteric Ca^{2+} activation constant [mM]	K_{d-Act}	2.56×10^{-4}	1.28×10^{-4}	-
Background Ca^{2+} leak [mS µF^{-1}]	G_{CaBk}	2.513×10^{-4}	7.539×10^{-4}	-
SR Ca^{2+} concentration dependent activation of SR Ca^{2+} release [mM]	EC_{50-SR}	0.45	0.5	-
Passive leak in the SR membrane [ms^{-1}]	K_{SRleak}	5.348×10^{-6}	1.07×10^{-5}	-
Velocity max for SR Ca^{2+} pump flux [mM ms^{-1}]	$V_{maxJpump}$	5.3114×10^{-3}	*	*
K_m SR Ca^{2+} pump forward mode [mM]	K_{mf}	2.46×10^{-4}	3×10^{-4}	-
K_m SR Ca^{2+} pump reverse mode [mM]	K_{mr}	1.7	2.1	-
L-type Ca^{2+} channel Ca^{2+} permeability [L F^{-1} ms^{-1}]	P_{Ca}	5.4×10^{-4}	8.91×10^{-4}	-
L-type Ca^{2+} channel Na^+ permeability [L F^{-1} ms^{-1}]	P_{Na}	1.5×10^{-8}	2.475×10^{-8}	-
L-type Ca^{2+} channel K^+ permeability [L F^{-1} ms^{-1}]	P_K	2.7×10^{-7}	4.455×10^{-7}	-
Background Ca^{2+} leak [mS µF^{-1}]	G_{CaBk}	2.513×10^{-4}	7.539×10^{-4}	-

Model term	Description
$i_{\mathrm{Cl(Ca)}}$	Ca^{2+}-activated chloride current
i_{Clb}	Background Cl current
i_{Cap}	SL-Ca^{2+} pump
i_{CaB}	Background Ca^{2+} leak
i_{NaB}	Background Na^{+} leak
i_{NaK}	NKA current
i_{tof}	fast Cardiac transient outward potassium
i_{tos}	slow Cardiac transient outward potassium
i_{Kr}	the 'rapid' delayed rectifier current
i_{Ks}	slowly activating K+ current
i_{K1}	inward rectifier K+ current
i_{Kp}	plateau potassium current
i_{kur}	slowly inactivating outward
i_{ss}	non-inactivating steady-state K+ current
i_{CaL}	LCC channel current
i_{NaCa}	NCX current
i_{Na}	Na^{+} current
SL_{Na}	SL Na^{+}
$jct1_{\mathrm{Na}}$	JSR Na^{+}
I	RyR inactive gate
O	RyR open gate
Cai	cytosolic Ca^{2+}
V	Action potential

Table S2: Model terms.

Table S3: Parameters used in SBM computational model to reflect control, hyperamylinemia/pre-diabetic rat, and control rabbit. Percentages in parentheses are relative to control rat. ^{I}from [6]. ^{II}from [29]. ^{III}fitted to [6]. ^{IV}fitted to [25].

Case	Sarcolemmal leak G_{Ca} (mS/μF)	SERCA V_{max} (mM/ms)	NKA I_{NKA_max} (μA/μF)
control	$^{II}7.5 \times 10^{-4}$	$^{IV}1.0 \times 10^{-2}$	$^{III}3.85$
+Amylin	$^{III}1.3 \times 10^{-3}$, (173%)	$^{III}1.0 \times 10^{-2}$	$^{III}4.40$, (114%)
HIP	$^{III}9.4 \times 10^{-4}$, (125%)	$^{III}6.2 \times 10^{-3}$,(62%)	$^{III}4.02$, (104%)
rabbit	$^{II}2.5 \times 10^{-4}$	-	-
rabbit+Amylin	7.5×10^{-4}	-	-

Table S4: Spearman correlations among analysis variables (N = 788) Note: *p-value < 0.05; **p-value < 0.01. Correlations in bold are between modeling inputs and outputs.

	1.	2.	3.	4.	5.	6.	7.	8.	9.	10.	11.
1. APD	1.000										
2. SR Ca^{2+}	**-0.296	1.000									
3. Ca^{2+} amplitude	**-0.168	**0.828	1.000								
4. diastolic Ca^{2+}	**-0.196	**0.792	**0.996	1.000							
5. cytosolic Na^{+}	**-0.106	**0.694	**0.699	**0.668	1.000						
6. Ca^{2+} transient decay (τ)	**0.149	**-0.717	**-0.361	**-0.299	**-0.598	1.000					
7. background Ca^{2+} leak	**-0.605	**0.600	**0.578	**0.586	**0.409	**-0.497	1.000				
8. background Na^{+} leak	**-0.111	**0.196	**0.166	**0.153	**0.457	**-0.115	0.000	1.000			
9. max NKA current	*0.073	**-0.318	**-0.284	**-0.269	**-0.611	**0.197	0.000	0.002	1.000		
10. LCC Ca^{2+} permeability	**0.495	**0.558	**0.568	**0.515	**0.340	**-0.378	0.000	0.000	0.000	1.000	
11. SERCA max velocity	**-0.171	**0.233	**-0.287	**-0.341	*-0.087	**-0.575	0.000	-0.001	0.001	0.000	1.000

S.3 Supplemental Results

S.3.1 L-type Ca^{2+} current measurement

L-type Ca^{2+} channel current (i_{Ca}) was measured under voltage-clamp in whole cell configuration (see Fig. S15). i_{Ca} was determined as the nifedipine-sensitive current recorded during depolarization steps from -40 mV (where the cell was held for 50 ms to inactivate Na^+ channels), to -35 to +60 mV (See Fig. S15). The patch-pipette was filled with a solution containing (in mM) 125 Cs-methanesulfonate, 16.5 TEA-Cl, 1 $MgCl_2$, 10 EGTA, 3.9 $CaCl_2$, 5 HEPES, and 5 Mg-ATP (pH=7.2). The external solution contained (in mM) 150 NMDG, 1 $CaCl_2$, 5 4-aminopyridine, 1 $MgCl_2$, 10 HEPES, and 10 glucose (pH=7.4).

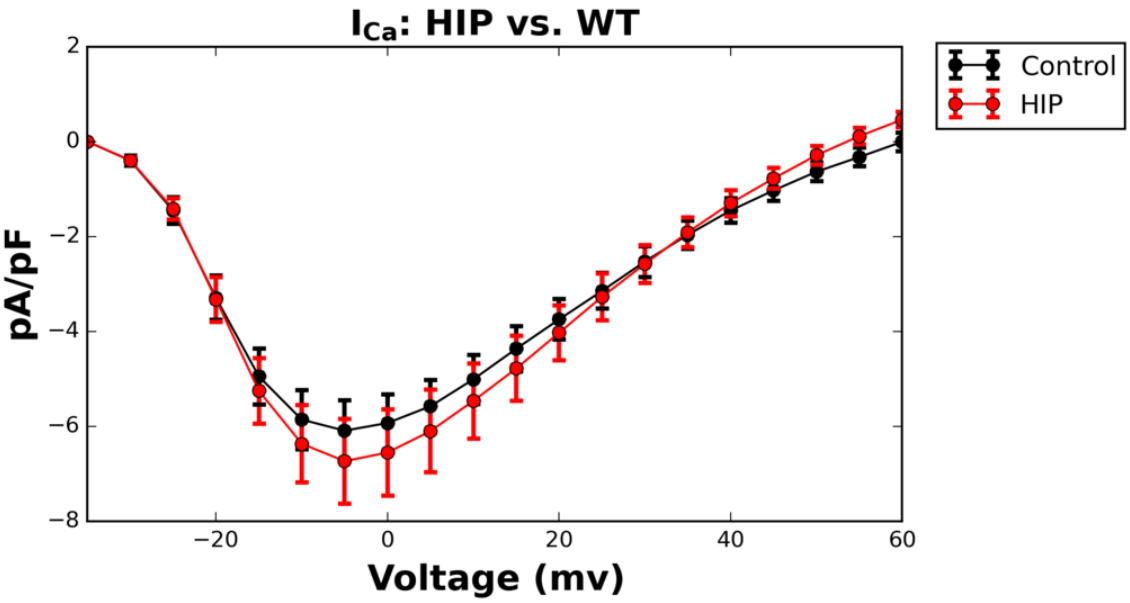

Figure S15: Experimental recordings of current versus applied voltage for the L-type calcium channel (LCC) in control (control) (n=8) and HIP (n=5) myocytes

S.3.2 Maintenance of sodium load

In the context of Ca^{2+} handling, Na^+ serves an important role in both extruding cytosolic Ca^{2+} in its 'forward' mode, as well as promoting Ca^{2+} influx during its brief 'reverse' mode [14]. Sodium load exceeding normal physiological ranges (approximately 9-14 mM in rodents), for instance, can contribute to diastolic dysfunction [64, 71], predominantly by impairing NCX Ca^{2+} extrusion [72]. Conversely, the NCX reverse mode may leverage Na^+ gradients to amplify sarcolemmal Ca^{2+} transients and thereby prime SR Ca^{2+} release [15, 22, 73–75].While our measurements of Na^+-load in +Amylin rats indicated that intracellular Na^+ was within normal ranges (Fig. S16), numerical predictions suggested that loading may be elevated under conditions of increased sarcolemmal Ca^{2+} leak with constant NKA function. Therefore to maintain predicted Na^+ transients within control levels, a modest increase in NKA V_{max} was predicted. On one hand, there is precedent for small peptides like insulin partitioning into the rat skeletal transverse tubule system [69], as well agonism of NKA activity due to amylin [30]. However, for rat cardiac ventricular tissues, these changes in NKA function may be non-existent or below the limits of experimental detection at least in fully-developed diabetes [76].

To further elucidate the potential contribution of NKA exchange to Ca^{2+} and Na^+ homeostasis, we present in Fig. S11 cytosolic and SR Ca^{2+} transient amplitudes as well as Na^+ load as a function of sarcolemmal leak rates and NKA activity. Our model assumes amylin does not change sarcolemmal Na^+ leak relative to control, therefore we attribute the positive correlation between Na^+ load and sarcolemmal Ca^{2+} leak to NCX exchange activity. Specifically, as cytosolic Ca^{2+} load increases with sarcolemmal leak rates, NCX exchange of cytosolic Ca^{2+} with extracellular Na^+ would contribute to increased intracellular Na^+. Analogously, as increased NKA activity depletes cytosolic Na^+, Ca^{2+} influx via the NCX reverse mode would be expected to decrease and thereby ultimately reduce intracellular Ca^{2+}. Our simulated data reflect these trends for several metrics of Ca^{2+} transients in Fig. S11a-c.

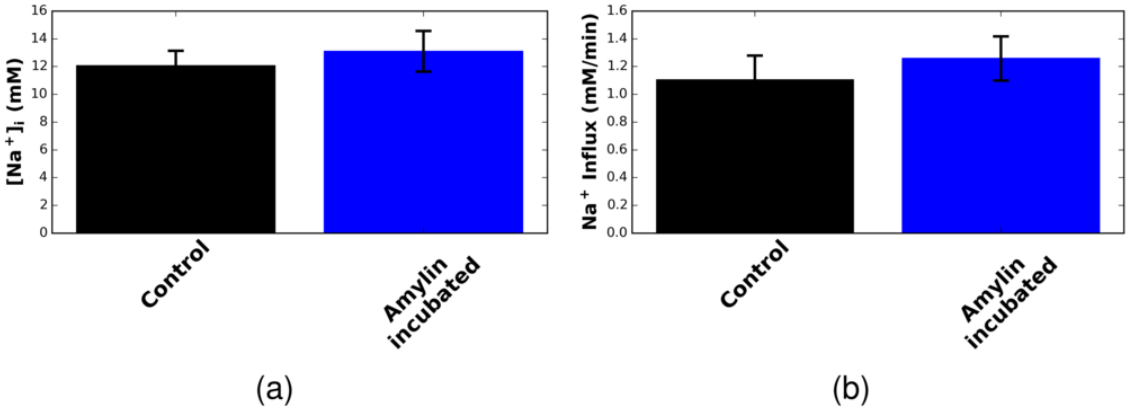

Figure S16: Experimental measurements of sodium load and influx in control myocytes (n=6) and myocytes incubated with human amylin(50 μM) for 2 hours (n=7). [6]

S.3.3 Validation of murine SB model

Potassium channel equations Among the most significant changes in the murine-specific Morotti model relative to the Shannon-Bers rabbit ventricular myocyte system are the phenomenological representations of K^+ channel currents. In Fig. S3 we compare time-dependent current profiles for nine of the prominent K^+ channels. Nearly all channels required minor parameter changes to correspond to murine species (i_{Kp},i_{NaK},i_{K1},i_{Kr},i_{tof}, i_{Ks}, and i_{tos}, of which the latter two were inactive in mice); however, two channels, i_{ss} and i_{kur}, were not included in the Shannon-Bers model and are thus implemented here. Following Morotti et al. [29], i_{ss} (Eq. S4d) and i_{kur} (Eq. S1a) were parameterized as follows:

IKur

$$i_{\text{Kur·PKAp}} = \frac{y_{174}}{i_{\text{KurtotBA}}} \tag{S1a}$$

$$a_{\text{Kur}} = \frac{0.2}{-1 + \frac{fI_{\text{KurpISO}}}{fI_{\text{Kurp·0}}}} \tag{S1b}$$

$$fIKuravail = 1 - a_{\text{Kur}} + \frac{a_{\text{Kur}}}{fI_{\text{Kurp·0}}} i_{\text{Kur PKAp}} \tag{S1c}$$

$$fIKuravail = 1 \tag{S1d}$$

$$i_{\text{kur1}} = G_{\text{kur·1}} K_{\text{coeff}} fI_{\text{Kuravail}} (-E_K + V) X_{\text{Kur slow}} Y_{\text{Kur slow1}} \tag{S1e}$$

$$i_{\text{kur2}} = G_{\text{kur·2}} K_{\text{coeff}} (-E_K + V) X_{\text{Kur slow}} Y_{\text{Kur slow2}} \tag{S1f}$$

$$i_{\text{kur}} = i_{\text{kur1}} + i_{\text{kur2}} \tag{S1g}$$

Xkur_gate

$$X_{\text{Kur slowss}} = \frac{1}{1 + 0.34e^{-71.4\times10^{-3}V}} \tag{S2a}$$

$$\tau_{\text{Xkur}} = 0.95 + 50\times10^{-3}e^{-80\times10^{-3}V} \tag{S2b}$$

$$\frac{dX_{\text{Kur slow}}}{dt} = \frac{1}{\tau_{\text{Xkur}}}\left(-X_{\text{Kur slow}} + X_{\text{Kur slowss}}\right) \tag{S2c}$$

Ykur_gate

$$Y_{\text{Kur slowss}} = \frac{1}{1 + 2.3\times10^{3}e^{0.16V}} \tag{S3a}$$

$$\tau_{\text{Ykur1}} = 400 - \frac{250}{1 + 553\times10^{-6}e^{-0.12V}} + 900e^{-\left(3.44+62.5\times10^{-3}V\right)^2} \tag{S3b}$$

$$\frac{dY_{\text{Kur slow1}}}{dt} = \frac{1}{\tau_{\text{Ykur1}}}\left(-Y_{\text{Kur slow1}} + Y_{\text{Kur slowss}}\right) \tag{S3c}$$

$$\tau_{\text{Ykur2}} = 400 + \frac{550}{1 + 553\times10^{-6}e^{-0.12V}} + 900e^{-\left(3.44+62.5\times10^{-3}V\right)^2} \tag{S3d}$$

$$\frac{dY_{\text{Kur slow2}}}{dt} = \frac{1}{\tau_{\text{Ykur2}}}\left(-Y_{\text{Kur slow2}} + Y_{\text{Kur slowss}}\right) \tag{S3e}$$

Xss_gate

$$xssss = X_{\text{Kur slowss}} \tag{S4a}$$

$$\tau_{\text{xss}} = 14 + 70e^{-\left(1.43+33.3\times10^{-3}V\right)^2} \tag{S4b}$$

$$\frac{dXss}{dt} = \frac{1}{\tau_{\text{xss}}}\left(-Xss + xssss\right) \tag{S4c}$$

$$i_{ss} = GssKcoeff\left(-E_K + V\right)Xss \tag{S4d}$$

In Fig. S2, we summarize several key predicted outputs for the Shannon-Bers (rabbit) and SBM (mouse) models: cytosolic and SR Ca^{2+} transients (a-b), as well as sodium load (c) and action potential (d). The SBM implementation exhibits, for instance, modestly higher Ca^{2+} transients in both the cytosol and SR, higher intracellular Na^{+} load and a significantly shorter AP, in comparison to data predicted for rabbit Ca^{2+} handling. The decreased action potential largely stems from reparameterization of the potassium currents defined above, the currents of which we summarize in Fig. S3. These model predictions are in quantitative agreement with corresponding current profiles presented in the Morotti *et al.* supplemental data [29], which were based on transient data from Dybkova *et al.* [70]. We present analogous current data for i_{Na}, i_{CaL}, and i_{NaCa}, which again are in quantitative agreement with Morotti *et al.*. Altogether, these predictions indicate that our implementation of the Morotti model faithfully reproduces the murine electrophysiology and Ca^{2+} handling. This implementation serves as the basis for our further refinement to reflect the rat Ca^{2+} dynamics.

S.3.4 Up-regulated SL currents (via LCC) relative to amylin incubation

The dominant effect of amylin appears to be its enhancement of non-selective SL Ca^{2+} currents, although there are reports that amyloidogenic peptides can alter LCC regulation [77]. To delineate this contribution from secondary agonism of SL Ca^{2+} channel activity, we performed simulations using an amplified i_{CaL} sufficient to reproduce the Ca^{2+} transients observed for enhanced SL Ca^{2+} leak. We emphasize here that LCC current/voltage relationship is indeed preserved in HIP rats (as shown in Fig. S15). Similar to +Amylin, increased LCC current yielded increased intracellular Ca^{2+} transients, elevated SR Ca^{2+} load, and increased diastolic Ca^{2+} load. Nevertheless, we identified distinct patterns of modulated channel activity for increased LCC relative to those presented for the +Amylin configuration. Namely, our models indicate amylin-induced Ca^{2+} leak amplifies i_{Na}, whereas in contrast, increased LCC conductance inflates the amplitudes of several prominent K^{+} channels. While the predicted channel currents have a complex dependence on ion-sensitive gating probabilities, these findings raise interesting possibilities that different modes of Ca^{2+} entry could in principle yield distinct influences on channels controlling the action potential. Nevertheless, under the conditions considered in this study, our modeling data (see Fig. S7 and Fig. S8) suggest that the modest perturbations in ion channel conductance under the +Amylin and LCC configurations did not

appreciably impact the APD. These findings are consistent with preserved APD upon P2X4 stimulation reported in Fig 6 of [50].

S.3.5 Genetic algorithm for fitting

We utilized a simple genetic algorithm (GA) to optimize model parameters to reproduce several experimental observables. We illustrate this procedure using NKA V_{max} optimization to improve agreement of our SBM-predicted Na^+ load with experimental measurements. 1) Given a 'reasonable' guess for the parameter, an ensemble (ca. 30) of lognormally distributed random variates are drawn, which serve to scale the parameter guess. The lognormal distribution was chosen to ensure that reductions and increases of N% were equally probable. 2) The SBM model is executed for each parameter variate, after which the observable, which in this case is the Na^+ intracellular concentration, is compared against the experimental value. 3) The concurrent of the model prediction with the experiment is assessed as a "job fitness" score

$$jobFitness_i = (X_{i,pred} - X_{expt})^2 \tag{S5}$$

3) The random variate presenting the best (smallest) job fitness score is then used as the parameter guess for subsequent optimization rounds. 4) The standard deviation, σ, used in the lognormal distribution is reduced with each iteration, j, to hone in on the best-fit parameter

$$\sigma_{j+1} = \sigma_0 e^{-i\sigma_j} \tag{S6}$$

Steps 1-4 are repeated until convergence, which we defined as

$$\lambda = \frac{\sqrt{jobFitness}}{X_{expt}} \tag{S7}$$

The tolerance parameter, λ, was typically below 1%. An example plot of the convergence of the NKA current value over number of iterations is shown in Fig. S6.

S.3.6 Comparison of parameter sensitivity

Sensitivity analyses Each parameter was randomized independently, while holding all other parameters at their default values for the rat model. The random draw was done within a standard deviation value of 10% of the given input value based on the baseline rat data, for a total of 150 random draws

for a given parameter. This process was repeated for each considered parameter to yield a total of 900 configurations. Descriptive statistics (mean (M), standard deviation (SD), median (med)), Spearman correlations, and plots (boxplots, scatterplots with LOESS curves) were initially performed to assess distributional characteristics and bivariate relationships between model inputs parameters and predicted outputs. Of particular interest were potential relationships between parameters corresponding to calcium background leak (`G_CaBk`) and NKA activity (`NaK_max`) and predicted outputs, including calcium and sodium transient amplitudes. Data were screened for outliers using Mahalanobis distance [78]. Multivariate analysis was performed with multivariate multiple regression and canonical correlation analysis [78], after rank transformations. All analyses were performed in SAS v9.4 (SAS Institute, Cary, NC). A two-sided p-value < 0.05 was considered statistically significant.

Sensitivity results Results additional to those reported in the main text are listed below. Inputs that had at least one significant association with any of the outputs included: Background Ca^{2+}leak ($\Lambda = 0.039$, F(5,49) = 242.804, $\eta^2 = 0.961$), background Na^{+}leak ($\Lambda = 0.009$, F(5,49) = 1,097.591, $\eta^2 = 0.991$), NKA V_{max} ($\Lambda = 0.001$, F(5,49) = 12,009.757, $\eta^2 = 0.999$), PCa ($\Lambda = 0.002$, F(5,49) = 5,906.809, $\eta^2 = 0.998$), T ($\Lambda = 0.002$, F(5,49) = 5,145.939, $\eta^2 = 0.998$), and SERCA V_{max} ($\Lambda = 0.014$, F(5,49) = 708.322, $\eta^2 = 0.986$). Thus, inputs respectively accounted for 96% or more variation in the best linear combination of outputs (all $\eta^2 \geqq 0.96$). Specifically for increasing Background Ca^{2+}leak and increasing background Na^{+}leak, there was only a significant association with increasing Nai (partial η^2 (η_p^2) = 0.568, $p < 0.001$ for CaBk and $\eta_p^2 = 0.829$, $p < 0.001$ for NaBk, respectively). Similar results were found for NKA V_{max}. Here, decreasing Nai was the only output that was significantly associated with increasing NKA V_{max} ($\eta_p^2 = 0.981$, $p < 0.001$). Increased PCa was significantly associated with both increased Nai ($\eta_p^2 = 0.929$, $p < 0.001$) and increased APD ($\eta_p^2 = 0.694$, $p < 0.001$). For T, higher Nai again was the only output significantly predicted by increasing T ($\eta_p^2 = 0.951$, $p < 0.001$), while T was also marginally significantly associated with SR Ca^{2+} ($\eta_p^2 = 0.058$, $p = 0.076$). Increased SERCA V_{max} was significantly associated with increased APD ($\eta_p^2 = 0.166$, $p = 0.002$), increased SR Ca^{2+} ($\eta_p^2 = 0.138$, $p = 0.005$), and decreased Nai ($\eta_p^2 = 0.354$, $p < 0.001$).

Multivariate associations were strong in magnitude and statistically significant for each input: background Ca^{2+} leak (Wilks $\Lambda = 0.160$, F(6,770) =

677.9, $p < 0.001$ partial η^2 (η_p^2) = 0.840), background Na^+ leak ($\Lambda = 0.146$, $F(6,770) = 758.9$, $p < 0.001$ $\eta_p^2 = 0.854$), max NKA current ($\Lambda = 0.094$, $F(6,770) = 1{,}243.0$, $p < 0.001$ $\eta_p^2 = 0.906$), LCC Ca^{2+} permeability ($\Lambda = 0.066$, $F(6,770) = 1{,}819.3$, $p < 0.001$ $\eta_p^2 = 0.934$), and SERCA max velocity ($\Lambda = 0.102$, $F(6,770) = 1{,}136.7$, $p < 0.001$ $\eta_p^2 = 0.898$). Follow-up canonical correlation analyses revealed that the best linear combination of outputs was almost perfectly correlated to the best linear combination of inputs ($r_1 = 0.977$, $p < 0.001$). In other words, for the model outputs we considered, one could with high confidence predict a linear combination of model outputs based on an appropriate linear combination of model parameters.

S.3.7 Ca^{2+} transient amplitudes following perturbation of cleft and SR Ca^{2+}

To investigate the contributions of cleft Ca^{2+} and SR Ca^{2+} variables on cytosolic Ca^{2+} transient amplitude output, we introduced negative and positive perturbations to these 'state' variables in our computational model, after which the maximum Ca^{2+} transient was recorded. This perturbation strategy permitted us to independently assess the contributions of the cleft and SR Ca^{2+} to cytosolic Ca^{2+} transients. Adjusting sarcolemmal Ca^{2+} leak as in our +Amylin and HIP simultaneously impact both Ca^{2+} pools among other states in the SBM model, which would otherwise obfuscate their independent contributions. A sample trajectory of one such perturbation is shown in Fig. S17a, while changes in cytosolic Ca^{2+} transient amplitude as a function of relative changes in cleft and SR Ca^{2+} are shown in the second panel. These data indicate that changes in SR Ca^{2+} account for the most significant changes in cytosolic Ca^{2+} transient amplitudes, while cleft Ca^{2+} also contributes but to a lesser degree.

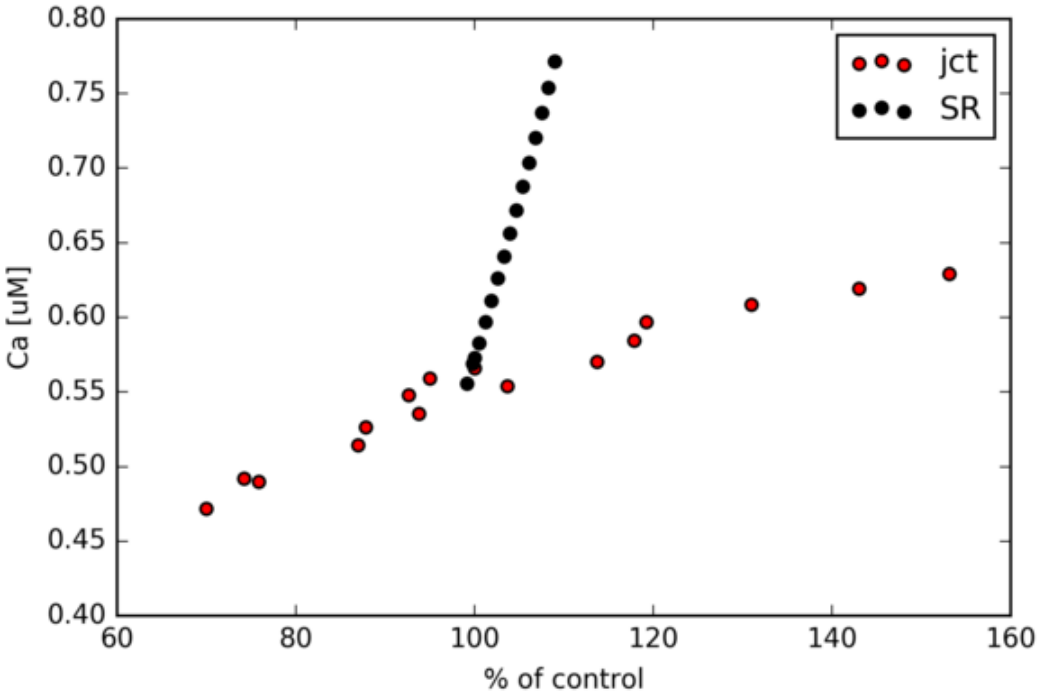

Figure S17: Predictions of cleft Ca^{2+} transient amplitude immediately following perturbation of cleft Ca^{2+} content (jct) or SR catwo content, following the protocol in Sect. S.3.7. Several trajectories for perturbed cleft Ca^{2+} are shown in Fig. S18.

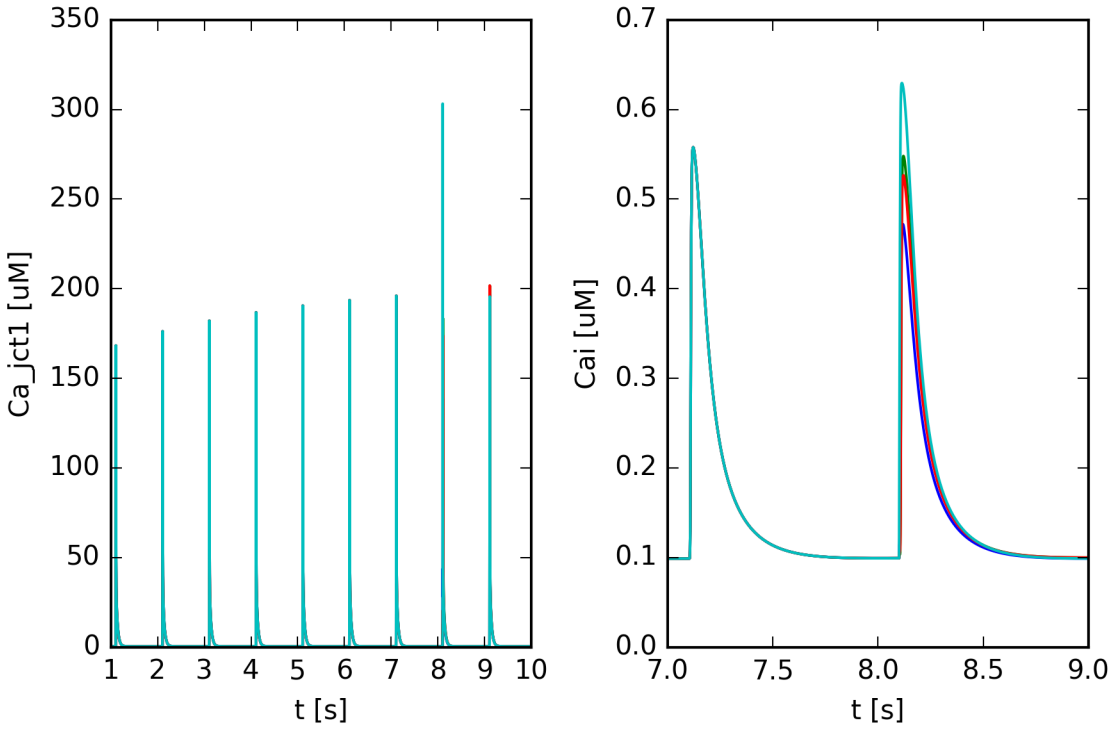

Figure S18: Time courses for predicted cleft and cytosolic Ca^{2+} transients, following randomized perturbations of the cleft Ca^{2+} near 8s.

S.4 nuclear factor of activated T-cells (NFAT) modeling

We implemented the Cooling *et al.* model of nuclear factor of activated T-cells (NFAT) signaling [63] into the SBM model, by implementing the following equations into the cytosolic compartment:

$$\frac{dCaCaM}{dt} = Ca_{\text{jct1}} kon_{\text{CaM}}(Bmax_{\text{CaM}} - Ca_{\text{CaM}}) \tag{S8}$$

$$- koff_{\text{CaM}} Ca_{\text{CaM}} \tag{S9}$$

$$\frac{dCaMCN}{dt} = CaCaMkon_{\text{CN}}(Bmax_{\text{CN}} - CaMCN) \tag{S10}$$

$$- koff_{\text{CN}} CaMCN \tag{S11}$$

$$fraction_{\text{CN}} = \frac{Ca^n_{\text{jct1}}}{Ca^n_{\text{jct1}} + kM^n_{\text{CaM}}(1 + \frac{^{kD}\text{CNCaM}}{^{CaM}\text{total}})} \tag{S12}$$

$$CN_{\text{active}} = CN_{\text{total}} fraction_{\text{CN}} \tag{S13}$$

$$NFAT_{\text{CytosolFlux}} = kon_{\text{NFATCytosol}} Ca_{\text{NFATCytosolInactive}} CN_{\text{total}} fraction_{\text{CN}} \tag{S14}$$

$$- koff_{\text{NFATCytosol}} Ca_{\text{NFATCytosolActive}}(1 - fraction_{\text{CN}} \tag{S15}$$

$$NFAT_{\text{CytosolNucleusFlux}} = Ca_{\text{NFATCytosolActive}} kOn_{\text{NFATCytosolNucleus}} \tag{S16}$$

$$NFAT_{\text{NucleusFlux}} = kon_{\text{NFATNucleus}} Ca_{\text{NFATNucleusActive}}(1 - fraction_{\text{CN}}) \tag{S17}$$

$$- koff_{\text{NFATNucleus}} Ca_{\text{NFATNucleusInactive}} CN_{\text{total}} fraction_{\text{CN}} \tag{S18}$$

$$NFAT_{\text{NucleusCytosolFlux}} = Ca_{\text{NFATNucleusInactive}} kOn_{\text{NFATNucleusCytosol}} \tag{S19}$$

NFAT concentrations following 5 min simulation time are reported in Fig. S19. It can be seen that as the increase in the diastolic Ca^{2+} and increased Ca^{2+} transient amplitude impacts the NFAT distributions. Namely, phosphorylated nuclear NFAT (nucNFATp) decreased overall given increases in Ca^{2+} diastolic load (HIP) and transient amplitude (+Amylin), while dephosphorylated cytosolic and nuclear NFAT (cytoNFAT* and nucNFAT*)

increased considerably. For the +Amylin and HIP cases, total nuclear NFAT content (nucNFAT_total) was increased, which parallel the increased nuclear/cytosolic NFAT ratio reported in Fig. 6D of [6].

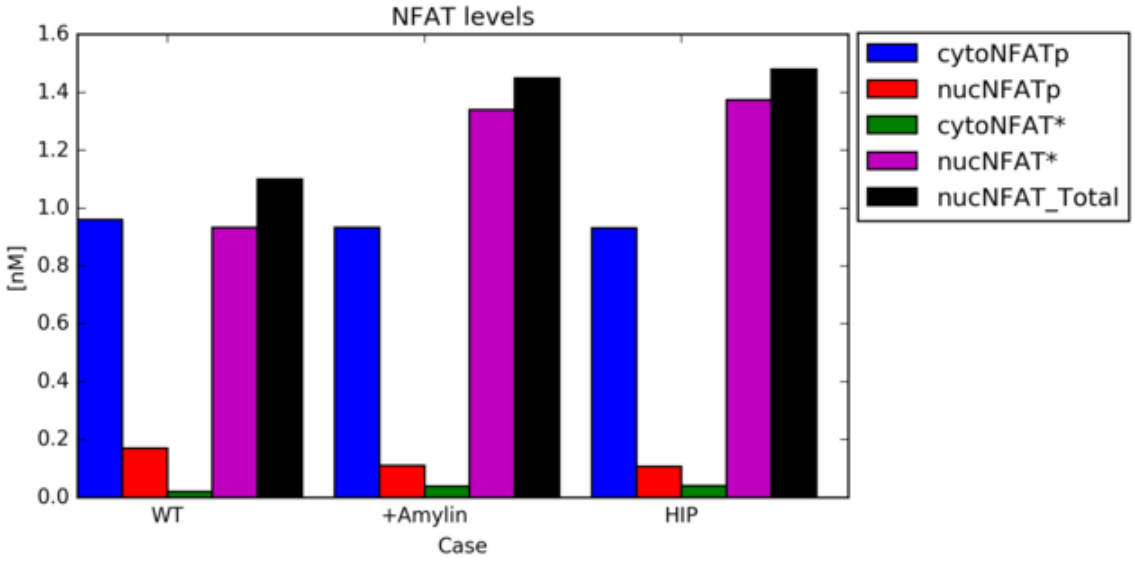

Figure S19: Predicted phosphorylated cytosolic and nuclear NFAT (cytoNFATp and nucNFATp, respectively), dephosphorylated NFAT (cytoNFAT* and nucNFAT*), and total nuclear NFAT content (nucNFAT_total), with respect to control, elevated diastolic and transient amplitudes for intracellular Ca^{2+}.